Propagation and Decay of Forced and Free Baroclinic Rossby Waves in Off-Equatorial Oceans*

BO QIU, WEIFENG MIAO, AND PETER MÜLLER

Department of Oceanography, University of Hawaii at Manoa, Honolulu, Hawaii

(Manuscript received 22 January 1997, in final form 16 April 1997)

ABSTRACT

Baroclinic Rossby wave motions in the off-equatorial oceans are investigated with emphasis on how eddy dissipation can influence the propagation of the height anomalies when both the forced wave response to wind in the interior ocean and the free wave response originating along the ocean's coastal and topographic boundaries are present. By explicitly estimating the decay scale for the long baroclinic Rossby wave, the authors show that the forced wave patterns at all off-equatorial regions appear to propagate westward at $2c_r$, where c_r is the phase speed of the long baroclinic wave. The presence of the boundary-generated, free Rossby waves in the low latitudes, however, reinforces the $1c_r$ phase propagation in the combined height anomaly fields. Toward higher latitudes, this reinforcement weakens as the boundary-generated, free waves become highly dissipative; as a result, the forced wave motion becomes more dominant, which works to increase the apparent phase speed up to $2c_r$. In the subpolar regions where the annual baroclinic Rossby waves become evanescent, an apparent phase speed higher than $2c_r$ is observed when an annual, standing wave response and a propagating wave response with an interannual frequency coexist. Stronger annual and interannual wind fluctuations over the Southern Hemisphere subpolar regions than over the Northern Hemisphere subpolar regions suggest that this coupling, and the phase speed higher than $2c_r$, are more likely to be detected in the Southern Hemisphere subpolar oceans.

1. Introduction

In a recent study, Chelton and Schlax (1996) conducted a thorough analysis of the satellite altimetric data from the first 3-year TOPEX/POSEIDON (T/P) mission. Focusing on the sea surface height (SSH) anomalies with wavelengths $\geq$500 km, Chelton and Schlax showed that the propagation speed of the observed SSH anomalies was in discord with the linear theory for free, first-mode baroclinic Rossby waves. They found that the linear theory predicts well the observed westward propagating phase speed only in the tropical band from 10°S to 10°N. Poleward of this band, the ratio of the observed phase speeds to the theoretical ones tends to increase monotonically from 1 to 2 in the Northern Hemisphere oceans and from 1 to 3 in the Southern Hemisphere oceans (see Fig. 1).

The presence of the first-mode, baroclinic Rossby waves in the low- and midlatitude oceans has been detected by many investigators based on upper-ocean temperature data and, more recently, on satellite altimetric data (e.g., White 1977, 1985; Meyers 1979; Kang and Magaard 1980; Kessler 1990; Jacobs et al. 1993, to cite the studies of the North Pacific Ocean alone). That the linear theory underestimates the phase speeds of the observed baroclinic Rossby waves was, in fact, previously noted by White (1977), Meyers (1979), and Kessler (1990) in their analyses of historical XBT/MBT data. As the domains of their analyses were confined, respectively, to the zonal bands from 10°N to 20°N and from 5°N to 22°N in the North Pacific, the generality of this discrepancy between the theory and observations was not clear. The analysis of the global T/P altimetric data by Chelton and Schlax (1996), for the first time, suggests that this discrepancy is universal, existing in both hemispheres of the Pacific, Atlantic, and Indian Oceans. In addition, recent analyses of simulated sea level fields from a global ocean general circulation model (OGCM) developed at the Los Alamos National Laboratory by Chelton (1996) and from the global OGCM of Chao and Fu (1995) by White et al. (1997) revealed very similar trends to that in Fig.1; namely, the westward phase speeds of the modeled SSH anomalies are systematically higher than the theoretical predicted values. Clearly, a robust, dynamic mechanism for this discrepancy must exist.

Several mechanisms have been suggested in the past that help explain the high phase speeds of the observed baroclinic Rossby waves. To explain the high phase speeds of the observed baroclinic Rossby waves found

* SOEST Contribution Number 4522.

Corresponding author address: Dr. Bo Qiu, Department of Oceanography, University of Hawaii at Manoa, 1000 Pope Road, Honolulu, HI 96822.
E-mail: bo@lunarmax.soest.hawaii.edu

© 1997 American Meteorological Society

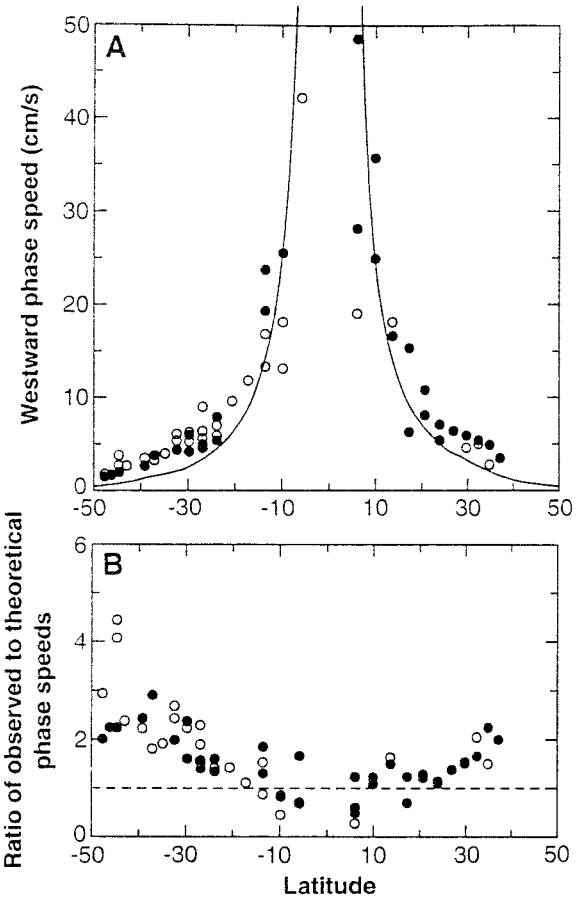

FIG. 1. (a) Phase speeds of westward propagating SSH anomalies estimated from 3 years of T/P altimeter data. Solid circles correspond to Pacific estimates, and open circles correspond to Atlantic and Indian Ocean estimates. Solid lines denote the theoretical phase speed of the long baroclinic Rossby waves averaged globally. (b) Ratio of the observed phase speeds to the theoretical values. [Both figures are taken from Chelton and Schlax (1996).]

in his XBT data analysis, White (1977) considered the ocean response under direct surface wind forcing. He showed that the ocean response in this case consisted of a directly forced component and a free, baroclinic Rossby wave component. A no-normal-flow condition along an eastern boundary yields an interior wave solution that propagates westward at a phase speed of $2g'\beta H_o/f^2$ $(=2c_r)$, or twice the speed of the free, baroclinic Rossby waves, where g' is the reduced-gravity constant, f the Coriolis parameter, β the meridional gradient of f, and H_o the mean upper-layer thickness. Although White's theory, which indicates that all wind-driven interior waves have twice the speed of the free waves, cannot explain all aspects of the observations revealed in Fig.1, it does suggest that the wind-driven response in an off-equatorial ocean is more complicated than the free wave response.

A more recent study by White et al. (1997) suggested that the oceanic Rossby waves are coupled with the overlying atmosphere. By analyzing the spatial phase relationship among the sea level, SST, and meridional surface wind data and using a simple coupled model, they demonstrated that a positive feedback exists between the oceanic and atmospheric variables, which works to increase (decrease) the westward phase speed of an oceanic Rossby wave poleward (equatorward) of the 25° latitude.

To account for the high phase speeds of the observed baroclinic Rossby waves, Killworth et al. (1997) considered the effects of background, baroclinic mean zonal flow upon the propagation of free baroclinic Rossby waves. By solving an eigenvalue problem for the vertical normal modes, they showed that inclusion of the mean zonal flow alters the background potential vorticity and works to increase the westward propagation of the free, baroclinic Rossby waves. Using the density profiles and the geostrophic shear flows calculated from the climatological temperature and salinity data (Levitus et al. 1994; Levitus and Boyer 1994), Killworth et al. showed that the theoretical phase speeds are similar to the observations and poleward of 30° they are several times faster than the linear theory without the mean flow would predict.

Another salient feature from Chelton and Schlax's (1996) study is that wave trains emanating from the west coast of the North American continent can be traced to cross the Pacific basin only in low-latitude regions (see their Fig. 4). Toward higher latitudes, the wave trains appear to be highly confined near the coast. In fact, Chelton and Schlax's Figs. 2a and 2b showed that most of the SSH anomalies observed along 39°N and 32°N originated in the middle of the ocean basin. This is in contrast to the signals along 21°N, where the SSH anomalies can be traced eastward to originate from the North American coast (their Fig. 2c).

That the boundary-originated baroclinic Rossby waves tend to dissipate rapidly offshoreward toward midlatitudes is also a common feature in numerical ocean modeling studies. Figure 2 shows an example from a 1½-layer, reduced-gravity model run, in which a zonal wind stress patch of annual frequency is applied over the equatorial Pacific centered at 170°E. The contours show a snapshot of the upper-layer thickness anomaly field after the model ocean reached a dynamically quasi-steady state. In this model, the baroclinic Rossby waves seen in the interior ocean are induced by the equatorial Kelvin waves (and the subsequent coastal Kelvin waves) excited by the oscillatory equatorial wind forcing. The confinement of the Rossby waves to the coast is obvious in midlatitudes. Although such a confinement has been commonly detected in observations and models, systematic studies on how dissipative forces will influence the propagation and decay of baroclinic Rossby waves are still lacking.

In this study, the theory of the forced ocean response put forth previously by White (1977) and other inves-

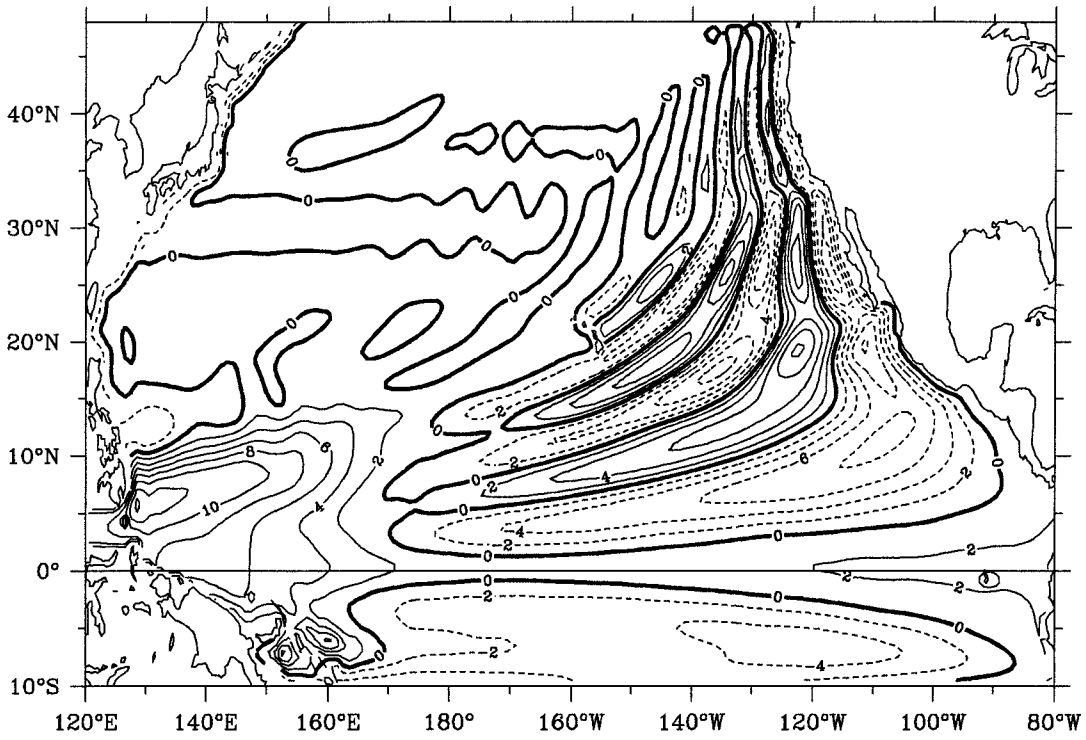

FIG. 2. Instantaneous upper-layer thickness anomaly field (in meters) derived from a nonlinear, 1½-layer reduced-gravity model. The model ocean has an initial constant depth of 300 m and is forced by an oscillatory zonal wind stress patch on the equator:

$$\tau^x = \begin{cases} \tau_o \cos[\pi(x - x_c)/L_x] \exp[-y^2/2L_y^2] \sin(\omega t), & -L_x/2 \le x \le L_x/2 \\ 0, & \text{otherwise,} \end{cases}$$

where $x_c = 170°$E, $L_x = 20°$ long, $L_y = 5°$ lat, $\omega = 2\pi/1$ yr, and $\tau_o = 0.1$ N m^{-2}. The model run reached a quasi-steady state after a 30-yr integration and the anomaly field shown here is from yr = 35. The horizontal eddy viscosity coefficient used in the model is $A_h = 500$ m^2 s^{-1}.

tigators will be extended in light of the observations summarized above. Notice that in addition to the eddy dissipation mechanism in the ocean's thermocline, vertical propagation of wave energy into the subthermocline ocean can also contribute to the disappearance of the boundary-originated Rossby waves (Kessler and McCreary 1993). The vertical propagation occurs in shorter distances at higher latitudes and longer distances at lower frequencies. In the present study, however, we will focus on the mechanism due to eddy dissipation. In particular, using a simple analytical model driven by idealized wind forcings, we will address the following questions: 1) Why does the free wave solution work well in low-latitude regions and why does the discrepancy between the theory and the observations become progressively greater with increasing latitude? 2) What roles do dissipative forces play in controlling the propagating pattern of the long baroclinic Rossby waves? 3) Can the ratio of the observed wave speeds exceed 2, as is suggested to be the case in the high-latitude, Southern Hemisphere oceans?

The presentation of this study is organized as follows. In section 2, we will consider the basic characteristics of free baroclinic Rossby waves. The focus is on the role of eddy dissipation in determining the propagation and decay of the free waves. Section 3 describes the basic features of the baroclinic Rossby waves forced in the interior ocean. The emphasis is again on the influence of eddy dissipation. In section 4 we will address the three questions raised above by considering more realistic cases in which both the boundary-generated free Rossby waves and the directly forced interior Rossby waves are present. A summary of the study is given in section 5.

2. Propagation and decay of free baroclinic Rossby waves

Like many previous studies, we will consider the baroclinic motion in a 1½-layer, reduced-gravity system in which the upper ocean of density ρ_1 exists above an infinitely deep, lower layer with a density ρ_2. Assuming the surface wind forcing acts as a body force upon the upper layer and the dissipation of motion is through horizontal eddy diffusion, the linear-

ized momentum and continuity equations can be written as follows:

$$\frac{\partial u}{\partial t} - fv = -g'\frac{\partial h}{\partial x} + \frac{\tau^x}{\rho_o H_o} + A_h\nabla^2 u \qquad (1)$$

$$\frac{\partial v}{\partial t} + fu = -g'\frac{\partial h}{\partial y} + \frac{\tau^y}{\rho_o H_o} + A_h\nabla^2 v \qquad (2)$$

$$\frac{\partial h}{\partial t} + H_o\left(\frac{\partial u}{\partial x} + \frac{\partial v}{\partial y}\right) = 0, \qquad (3)$$

where (u, v) are the (x, y) components of the horizontal velocity, (τ^x, τ^y) the (x, y) components of the surface wind stress vector, h the upper-layer thickness, H_o the mean upper-layer thickness, $g' = (\rho_2 - \rho_1)g/\rho_o$ the reduced gravity, A_h the coefficient of horizontal eddy viscosity, ∇^2 the horizontal Laplacian operator, and f the Coriolis parameter. Although we have assumed the dissipation in the form of horizontal eddy diffusion in Eqs. (1) and (2), expressing the dissipation in other forms, such as Newtonian momentum damping, will not qualitatively change the results presented below (see the appendix).

Cross-differentiating Eqs. (1) and (2) and eliminating the velocity divergence from the continuity equation leads to the vorticity equation. Under the low-frequency and quasigeostrophic assumptions (for a detailed discussion of these assumptions, see McCreary 1977), the vorticity equation simplifies to

$$\frac{\partial}{\partial t}(h - \lambda^2\nabla^2 h) - c_r\frac{\partial h}{\partial x} + A_h\lambda^2\nabla^2(\nabla^2 h) = -\nabla \times \left(\frac{\boldsymbol{\tau}}{\rho_o f}\right), \qquad (4)$$

where $\lambda = \sqrt{g'H_o}/f$ is the baroclinic Rossby radius, and $c_r = \beta\lambda^2$ is the speed of free baroclinic Rossby waves (with β being the meridional gradient of f). Assuming a wave solution of $h \sim \exp(i\omega t - ikx - ily)$ in the homogeneous part of Eq. (4) gives the dispersion relation:

$$\omega\left(k^2 + l^2 + \frac{1}{\lambda^2}\right) + \beta k - iA_h(k^2 + l^2)^2 = 0. \qquad (5)$$

Notice that if we are interested in the waves with length scales of $O(10^\circ)$ or longer (which is the case in analyzing altimetrically measured SSH data), the long-wave approximation is valid: $k^2, l^2 \ll \lambda^{-2}$. We may not, however, ignore k^2 or l^2 in the third term of Eq. (5) associated with the vorticity dissipation. In other words, the vorticity equation with dissipation is y dependent even under the long-wave approximation.

For typical values of the baroclinic Rossby waves of our interest, namely, $\omega \le 2\pi/(1\text{ yr})$, $c_r = 0.01$–0.1 m s^{-1}, and $A_h = 500$–2500 m^2 s^{-1}, it is straightforward to show from Eq. (5) that the zonal wavenumber k is

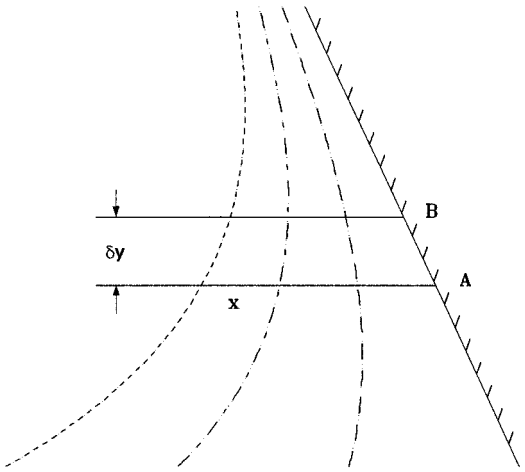

FIG. 3. A schematic showing the phase propagation along two parallels *A* and *B*. Dashed lines show constant phase lines; the phase difference along the coast may be neglected if the time for the coastal Kelvin waves to travel δy from **A** to **B** is much shorter than the forcing period.

$$k = k_b\left[1 - \frac{4A_h^2}{\beta^2}(l^2 + k_b^2)^3\right] + i\frac{A_h}{\beta}(l^2 + k_b^2)^2 + O\left[\frac{A_h^3}{\beta^3}k_b^2(l^2 + k_b^2)^4\right],$$

where $k_b = -\omega/c_r$ is the wavenumber of the *nondissipative*, long baroclinic waves. For the parameter regime of our interest, $4A_h^2(l^2 + k_b^2)^3/\beta^2 \ll 1$, so

$$k \approx k_b + i\frac{A_h}{\beta}(l^2 + k_b^2)^2, \qquad (6)$$

indicating that the westward phase speed of the *dissipative*, long baroclinic waves, $\omega/\mathrm{Re}(k)$, will remain the same as its nondissipative value c_r.

In order to find the decay scale of the dissipative baroclinic waves, we need to evaluate l in Eq. (6). This can be done by considering the baroclinic waves emanating from the eastern boundary of an ocean basin (due to either oscillating alongshore winds or baroclinic Kelvin waves generated along the equator). Focusing on the two points **A** and **B** separated by δy along the coast (see Fig. 3), we will assume the initial phase of the waves at these two points to be equal. This assumption is reasonable if the phase difference is much shorter than the wave period of interest. For the coastal Kelvin waves under consideration, this assumption is well valid. At a given offshore location x, the time difference between the arrival of the initial phase line is

$$\delta t = \frac{x}{c_B} - \frac{x}{c_A} \approx \frac{x}{\beta g' H_o}(f_B^2 - f_A^2) \approx \frac{2xf}{g'H_o}\delta y,$$

where c_A is the zonal phase speed of the dissipative baroclinic waves at latitude A (recall that eddy dissipation does not alter the zonal phase speed of the bar-

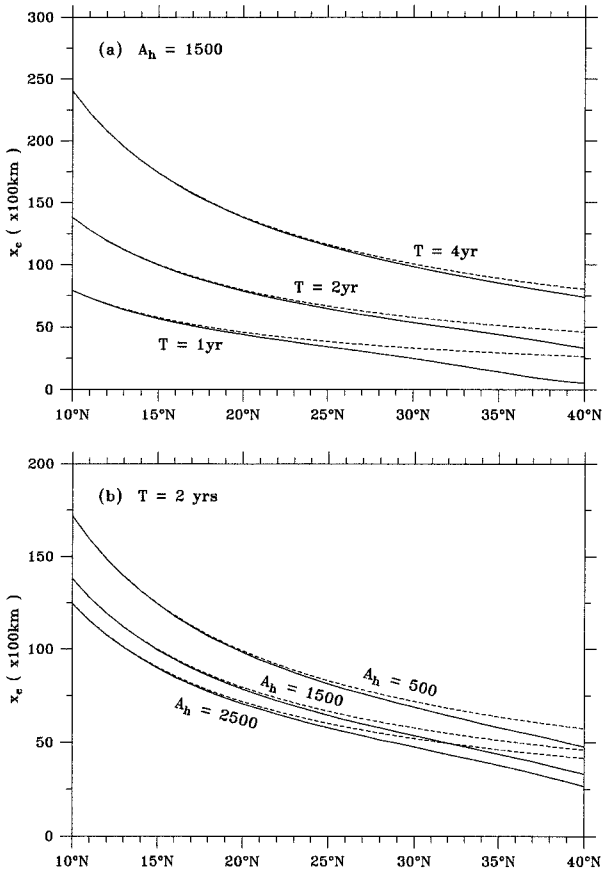

FIG. 4. The *e*-folding decay scale x_e as a function of latitude. In (a) the eddy viscosity coefficient is fixed at 1500 m^2 s^{-1}, while the wave period is altered. In (b) the wave period is fixed at 2 yr, but with different A_h values. In both figures, dashed lines denote the approximate solution of (9) and solid lines denote the exact solution from Eq. (8). For all cases, $g'H_o = 8.1$ m^2 s^{-2}.

oclinic waves, so $c_A \sim c_{rA} = \beta g' H_o / f_A^2$). Using the definition for l and the above relation, we have

$$l = \frac{\omega}{c_{py}} = \frac{\omega \delta t}{\delta y} = \frac{2\omega\beta}{f c_r} x, \tag{7}$$

where c_{py} is the meridional phase speed. Substituting l in (6), we can estimate the *e*-folding distance x_e of the decaying baroclinic Rossby waves by solving

$$\frac{A_h}{\beta} \int_0^{x_e} (l^2 + k_b^2)^2 \, dx = -1$$

or

$$\frac{A_h \omega^4}{\beta c_r^4} \int_0^{x_e} \left[\left(\frac{2\beta x}{f} \right)^2 + 1 \right]^2 dx = -1. \tag{8}$$

Figure 4a shows the x_e values as a function of latitude for different ω for the North Pacific. Clearly, the higher the latitude the waves emanate from, the shorter their *e*-folding scales become. In the region where x_e is relatively large (i.e., $x_e \gg f/2\beta = R \tan\theta/2$, where R is radius of the earth and θ the latitude), the *e*-folding scale can be approximated by

$$x_e \approx -\left[\frac{5\beta (g' H_o)^4}{16 \omega^4 A_h f^4} \right]^{1/5} \tag{9}$$

(see dashed lines in Fig. 4a). Notice that the *y*-dependence of x_e is proportional to both $f^{-4/5}$ and $\omega^{-4/5}$. Also notice that under this approximation, $x_e \sim A_h^{-1/5}$, suggesting that the *e*-folding scale is not very sensitive to the A_h value. Changing A_h by tenfold will only alter the *e*-folding scale by 15%. Toward higher latitudes [where Eq. (9) is less valid], however, the *e*-folding scale does become more sensitive to changes in A_h. A recent study by Jenkins (1991) based on tritium–helium observations in the main thermocline of the Sargasso Sea indicated $A_h = 1840 \pm 440$ m^2 s^{-1}. In the following discussion, we will consider A_h in the range from 500 to 2500 m^2 s^{-1}.

In Fig. 5, the theoretical *e*-folding scale x_e is superimposed upon the rms amplitudes of the upper-layer thickness anomalies derived from the model simulation shown in Fig. 2. The theoretical values (the pluses) follow well the 1.0-m contours of the rms amplitude, suggesting that despite the fact that the numerical model is governed by a more complicated set of physics, including nonlinear advection and wave dispersion, the simple theory developed above accounts well for the decay scale of the boundary-generated, free long baroclinic Rossby waves.

3. Propagation and decay of forced baroclinic Rossby waves

One point worth emphasizing from the preceding section is that the baroclinic signals originating along the eastern boundary in mid and high latitudes will not survive their journey across the Pacific Ocean (which has a width of more than 12 000 km). In other words, toward higher latitudes, the baroclinic wave motions will be increasingly dominated by those induced directly within the ocean's interior. To understand the wave motions there, we need to look into the characteristics of the *forced* baroclinic Rossby waves. To do so, it is intuitive to consider the case in which the wind-driven Ekman convergence term in the vorticity equation (4), $-\nabla \times (\boldsymbol{\tau}/\rho_o f)$, has a simple temporal and spatial pattern. Specifically, we assume this forcing term oscillates at a frequency ω_f and has a constant amplitude A_o within the zonal band $x_b \le x \le 0$:

$$-\nabla \times \left(\frac{\boldsymbol{\tau}}{\rho_o f} \right) = \begin{cases} A_o \cos(\omega_f t), & x_b \le x \le 0 \\ 0, & \text{otherwise.} \end{cases} \tag{10}$$

Without loss of generality, we have set $x = 0$ at the eastern edge of the forcing band (notice that this edge does not have to coincide with the ocean's eastern boundary). To simplify the argument, we will further restrict the attention to the zonal propagation of the *h* anomaly field, as this is the quantity commonly analyzed

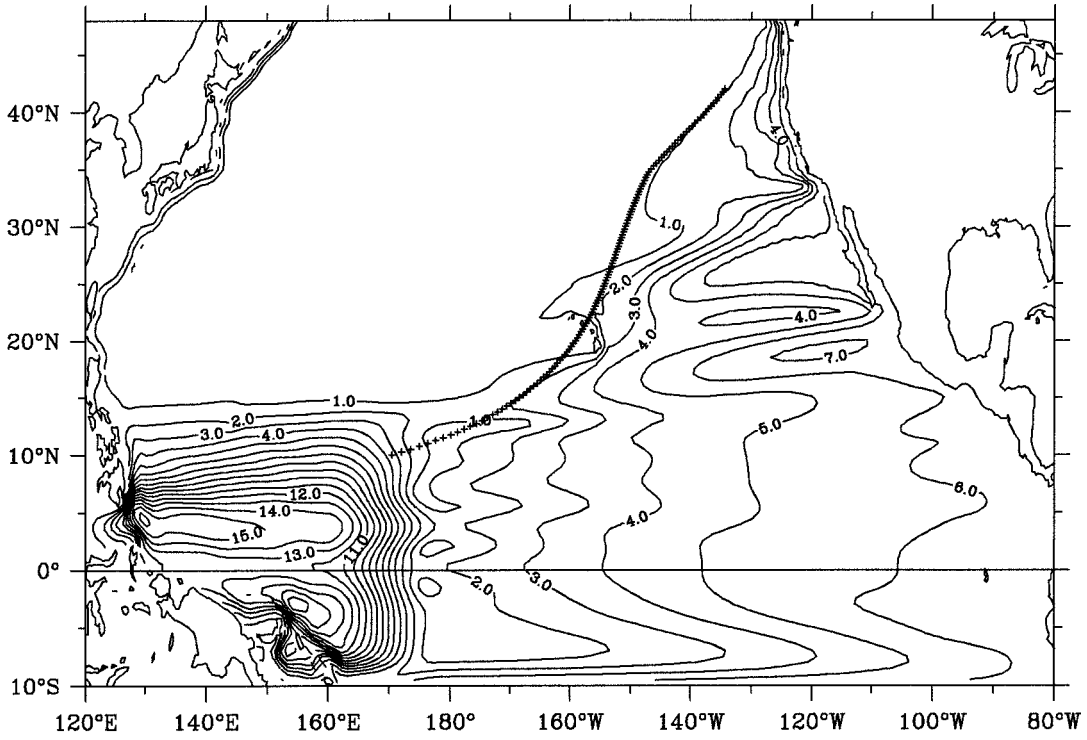

FIG. 5. Rms amplitudes (in meters) derived from the numerical model run shown in Fig. 2. Large amplitude fluctuations in the western equatorial region are due to the forcing of the oscillatory wind stress patch there. Fluctuations offshore of the North American continent are results of the baroclinic Rossby waves emanating from the eastern boundary. Pluses indicate the *e*-folding decay scale based on Eq. (8) for the baroclinic Rossby waves initiated along the eastern boundary.

from the observational data. Thus, no y dependence will be explicitly included below.

Due to the long-wave approximation, the area east of the forcing band is unperturbed:

$$h = 0 \quad \text{for } 0 \le x. \tag{11}$$

(This solution is valid even when wave dispersion is allowed, as the baroclinic Rossby waves with eastward group velocity are highly sensitive to dissipation, due to their shorter wavelengths.) Within the forcing band, the solution of Eq. (4) is the sum of a standing wave and a traveling wave:

$$h = \frac{A_o}{\omega_f}[\sin(\omega_f t) - e^{-x/x_e}\sin(\omega_f t - k_b x)] \quad \text{for } x_b \le x \le 0. \tag{12}$$

As noted by White (1977), the amplitude of the traveling wave matches that of the standing wave in order to satisfy the boundary condition at $x = 0$.

West of the forcing band, the solution constitutes two traveling waves emanating from the eastern and western edges of the forcing band, respectively:

$$h = \frac{A_o}{\omega_f}e^{-x/x_e}\{e^{x_b/x_e}\sin[\omega_f t - k_b(x - x_b)] - \sin(\omega_f t - k_b x)\} \quad \text{for } x \le x_b. \tag{13}$$

Here, the amplitude of the traveling wave emanating from the western edge has been determined by the continuity condition of h at $x = x_b$. It is clear from (13) that the h anomalies west of the forcing band will propagate westward at the free baroclinic Rossby wave speed $c_r = \omega_f/k_b$. Although the phase of the h contours depends on the relative size of x_e versus x_b, there exists no ambiguity about the phase speed in the combined wave field.

This, however, is not the case for the h pattern within the forcing band. Estimating the phase speed from the h anomaly pattern given by (12) can be subtle. To see this, we nondimensionalize x, t, and h by $1/k_b$, $1/\omega_f$, and A_o/ω_f. This simplifies (12) to

$$h^* = \sin(t^*) - e^{-x^*/x_e k_b}\sin(t^* - x^*), \tag{14}$$

where the asterisk denotes nondimensional quantities. From (14), it is clear that the h^* field depends on a nondimensional parameter $x_e k_b$, or the ratio of the *e*-folding decay scale to the zonal scale of the Rossby waves $1/k_b$. Figure 6 shows the h^* patterns as a function of the non-

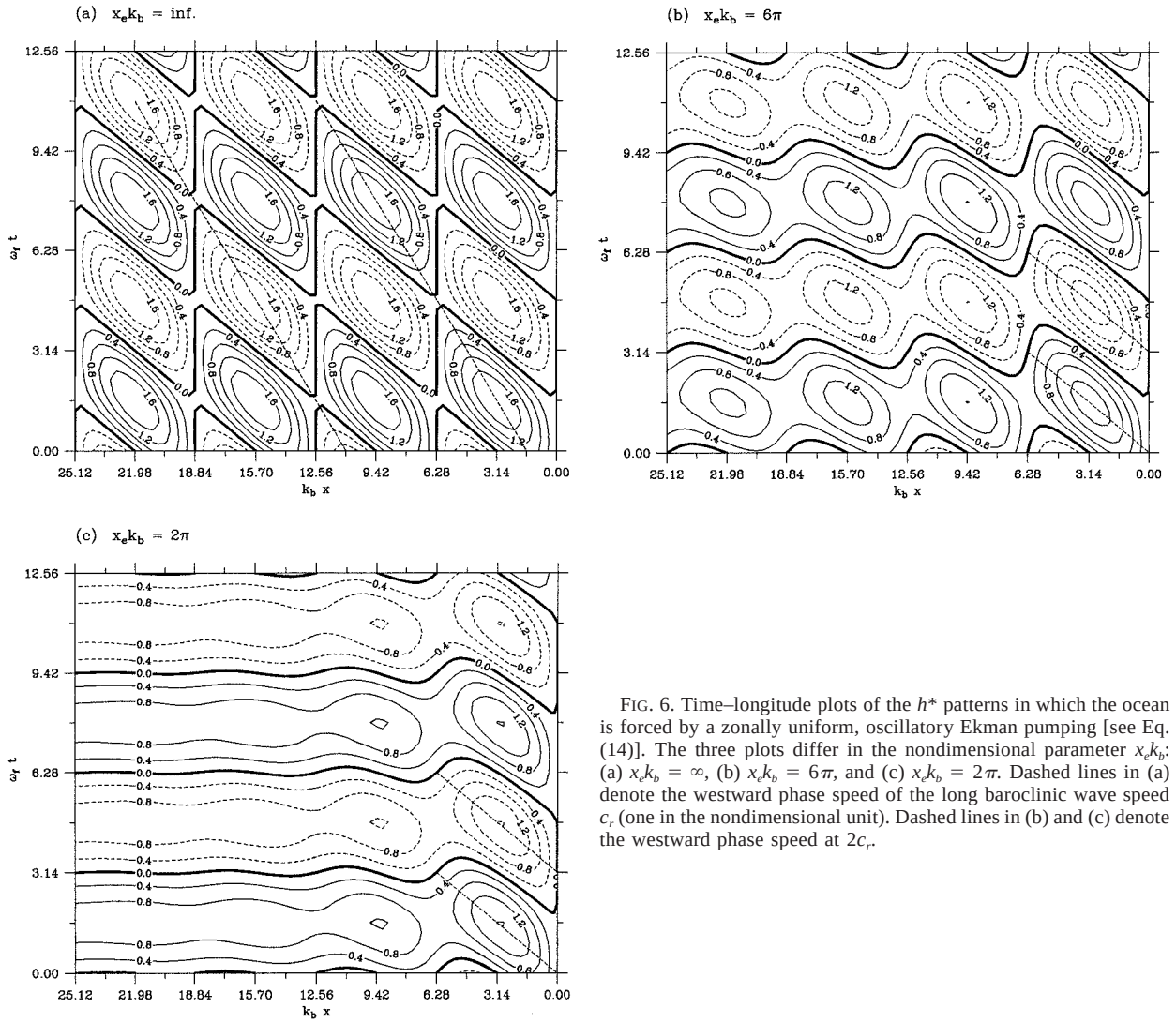

FIG. 6. Time–longitude plots of the h^* patterns in which the ocean is forced by a zonally uniform, oscillatory Ekman pumping [see Eq. (14)]. The three plots differ in the nondimensional parameter $x_e k_b$: (a) $x_e k_b = \infty$, (b) $x_e k_b = 6\pi$, and (c) $x_e k_b = 2\pi$. Dashed lines in (a) denote the westward phase speed of the long baroclinic wave speed c_r (one in the nondimensional unit). Dashed lines in (b) and (c) denote the westward phase speed at $2c_r$.

dimensional time and space for $x_e k_b = \infty$, 6π, and 2π. In the nondissipative limit ($x_e k_b \to \infty$), Eq. (14) can be rewritten as

$$h^* = 2 \sin\left(\frac{x^*}{2}\right) \cos\left(t^* - \frac{x^*}{2}\right), \qquad (15)$$

a result presented previously by White (1977) and other investigators. Although Eq. (15) appears to suggest that the h^* anomalies propagate at twice the phase speed of a free baroclinic wave, Fig. 6a shows that connecting the positive or negative anomalies over several wavelengths results in a phase speed the same as that of a free wave (or, unity in the nondimensional unit). This is simply due to the fact that the ''doubled-phase-speed wave'' in Eq. (15) is modulated by a sine function whose horizontal scale is the same as that of the doubled-phase-speed wave.

When dissipation is present, Eq. (14) indicates that the traveling wave component will be damped selectively as the signal moves westward, whereas the standing wave component remains unaffected. The resultant h^* pattern in this case can be visually quite different from the nondissipative case. As shown in Figs. 6b and 6c, the doubled-phase-speed pattern stands out more apparently as $x_e k_b$ decreases. Notice that though appearing to move westward at $2c_r$, the traveling wave anomalies initiated at the eastern edge of the forcing band propagate westward at *one* free wave speed.

In Fig. 7, we plot the $x_e k_b$ values as a function of latitude and the eddy viscosity coefficient under the forcing of an annual frequency. For a given A_h value, $x_e k_b$ attains its maximum somewhere in the midlatitude. Poleward of that latitude, $x_e k_b$ decreases due to the shortening of the e-folding scale; equatorward, it decreases due to the lengthening of the zonal scale of the baroclinic Rossby waves. Except for very low A_h values, most of $x_e k_b$ fall below 6π, suggesting the

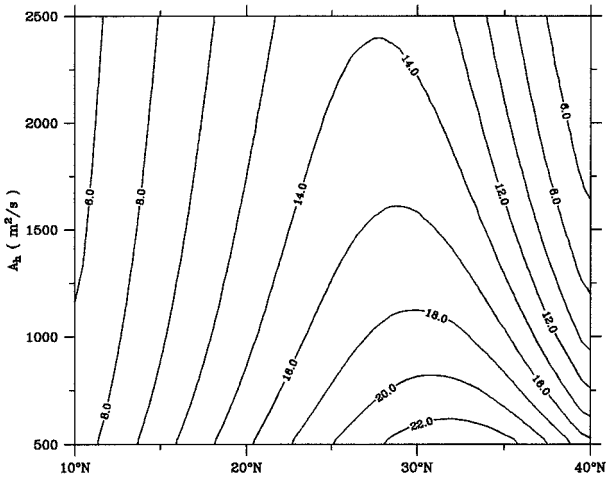

FIG. 7. Values of $x_e k_b$ as a function of latitude and the horizontal eddy viscosity coefficient. Physically, $x_e k_b$ gives the ratio of the long baroclinic Rossby wave's decay scale to the wave's length scale.

combined h^* pattern of the standing wave and the dissipative traveling wave would, at all latitudes, appear to move westward at $2c_r$.

4. Discussion

a. *Latitudinal dependence of the phase speed of combined forced and free waves*

In the real ocean, Rossby waves are generated both within the interior ocean due to direct wind forcing and along the eastern boundary due to either alongshore wind fluctuations or equatorial-originated coastal Kelvin waves. Although the forced wave motion, as we noted in the previous section, would appear at all latitudes to move westward at twice the free wave speed, its blending with the boundary-generated free Rossby waves can change the apparent speed of the h^* anomalies in an x–t plot. To see this, let us add a boundary-generated, free wave solution to (14):

$$h^* = \alpha^* e^{-(x^*-x_a^*)/x_e k_b} \sin(t^* - x^* + \theta^*) + \sin(t^*) - e^{-x^*/x_e k_b} \sin(t^* - x^*), \quad (16)$$

where the first term on the rhs denotes the free wave solution with α^* being its amplitude nondimensionalized by A_o/ω_f, θ^* its phase relative to that of the forced wave, and x_a^* being the position of the boundary (recall that $x^* = 0$ is the eastern edge of the forcing band). Notice that although the term ''boundary'' above has been narrowly defined to be the eastern boundary of an ocean basin, it can represent other geographical locations where free, baroclinic Rossby waves are generated. Midocean ridges and seamounts are good examples along which baroclinic Rossby waves can be excited due to interaction between the mean flow and the topography (e.g., Barnier 1988; Wang and Koblinsky 1994).

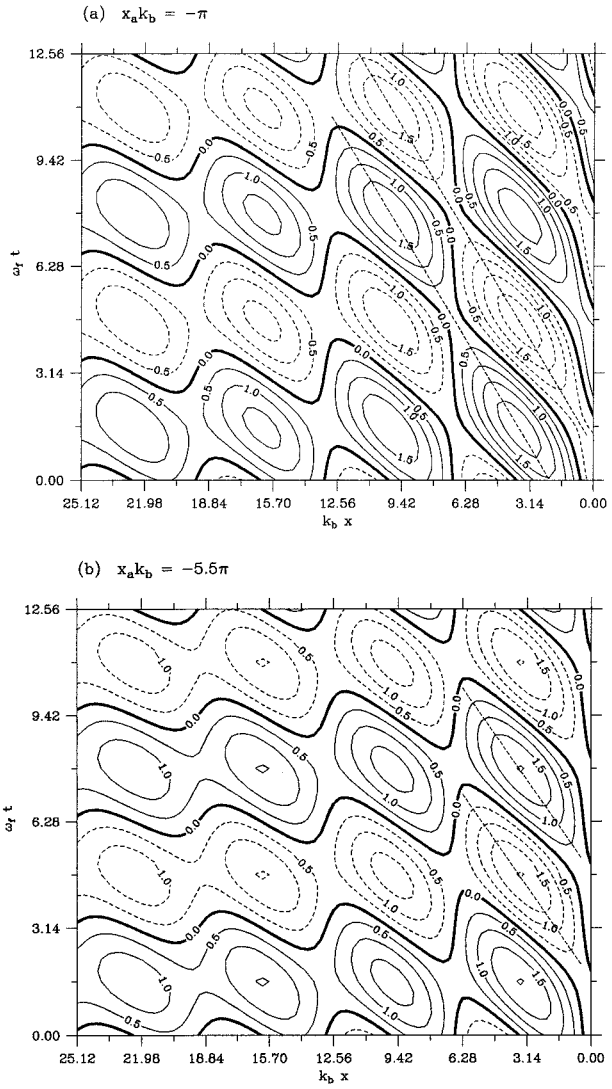

FIG. 8. Time–longitude plots of the h^* patterns in which a boundary-generated free wave is superimposed on a forced solution [see Eq.(16)]. In (a), the origin of the free wave is relatively close to the eastern edge of the forced motion, $x_a k_b = -\pi$, whereas in (b), it is comparable to the baroclinic wave's decay scale, $x_a k_b = -5.5\pi$. For both cases, $x_e k_b = 6\pi$, $\theta^* = 0.4\pi$, and $\alpha^* = -1.2$. Dashed lines in (a) denote the westward phase speed at c_r and those in (b) at $1.2c_r$.

Figure 8a shows a typical h^* pattern based on (16) when x_a is relatively small compared to the decay scale of the free wave x_e (i.e., $x_a k_b = -\pi$ vs $x_e k_b = 6\pi$). In other words, it represents the situation in which the boundary-generated free wave is not quite dissipated when it reaches $x^* = 0$. Because the boundary-generated free wave propagates at c_r, Fig. 8a shows that its presence works to reinforce the connection between the positive (or negative) h^* anomalies, which, in the forced solution (14), was disrupted due to the decay of the traveling wave component (Figs. 6b and 6c). Connecting the positive (or negative) anomalies in Fig. 8a results in a westward phase

speed close to $1c_r$. Notice that the reinforcement occurs when $\alpha^* \cos\theta^* < 0$, that is, when the boundary-generated free wave has the same sign as the traveling wave of the forced solution [the third term on the rhs of (16)].

When the scale of x_a (the distance between the origin of the boundary-generated, free wave and the eastern edge of the wind forcing) becomes comparable to x_e, the influence of the boundary-generated Rossby wave upon the forced solution becomes weaker and the combined h^* solution of (16) will exhibit westward propagation at a speed between $1c_r$ and $2c_r$. Figure 8b shows the combined h^* pattern when $x_a/|x_e| = 0.92$ (the other parameters were kept the same as in Fig. 8a); the phase speed of the combined h^* pattern from this example is $1.2c_r$. Though its exact value depends on the chosen parameters, the phase speed of the combined h^* pattern from (16) always falls within the $1c_r$ to $2c_r$ range. If x_a becomes much greater than x_e, the boundary-generated, Rossby wave will have little effect on the forced solution; the combined h^* solution of (16) in this case will remain the same as those presented in Fig. 6. In other words, the h^* pattern will appear to move westward at $2c_r$.

Because x_e in the ocean decreases monotonically with latitude (e.g., see Fig. 4), the result presented above suggests that the height anomaly patterns at low latitudes are likely to propagate at $1c_r$ because of the strong presence of the boundary-generated, free Rossby waves. Toward higher latitudes as the influence of the boundary-generated Rossby waves diminishes, the forced wave motion becomes more dominant and this increases the apparent phase speed of the height anomalies up to $2c_r$. The result from this simple argument is in accord with the trend found by Chelton and Schlax (1996) that the phase speed of the observed SSH anomalies increases progressively from $1c_r$ to $2c_r$ in the subtropical oceans (10°–35° lat band).

b. *Can the phase speed of combined waves exceed $2c_r$?*

Beyond 35° lat, Chelton and Schlax's analysis indicated that the phase speed of the observed SSH anomalies can exceed $2c_r$ (Fig. 1). Such a high phase speed can be explained by extension of the above theory in the following way. Although the wind fluctuations over the ocean are dominated by the annual signals, interannual wind fluctuations can be equally important for baroclinic wave motions. This is particularly true in subpolar regions where the baroclinic Rossby waves with an annual period become evanescent [in the subpolar North Pacific, e.g., the annual baroclinic Rossby waves become evanescent around 40°N, McCreary et al. (1987)]. Using the monthly ECMWF wind stress data from 1985 to 1995, we plot in Figs. 9a and 9b the rms amplitudes of the surface wind stress curl fluctuations in the annual and biennial frequency bands, respectively. In general, the biennial wind fluctuations have a rms amplitude half that of the annual signals. The largest biennial fluctuations are found over the subpolar oceans. Unlike the annual Rossby waves, the baroclinic waves with the biennial frequency can exist as traveling waves there.

When both annual and biennial wind forcings are present in subpolar regions, the baroclinic response induced by the annual wind is dominated by the standing wave component $\sin t^*$ and the influence from the evanescent wave component can be neglected. As a result, the combined response due to the annual and biennial winds in this case can be expressed by

$$h^* = \alpha^* \sin(t^* + \theta^*) + \sin\left(\frac{t^*}{2}\right) - e^{-x^*/x_e k_b} \sin\left(\frac{t^*}{2} - \frac{x^*}{2}\right), \quad (17)$$

where the first term on the rhs denotes the standing wave component due to the annual forcing and the second and third terms denote the wave solution due to the biennial forcing [cf. Eq. (14)]. In Eq. (17), α^* is the amplitude of the annual standing wave relative to the biennial standing wave, and θ^* denotes the phase difference between these two wave components. Figure 10 shows a typical h^* pattern derived from (17). That the h^* pattern in this case appears to propagate westward at $3c_r$ is no surprise. Combining a standing wave solution of an annual frequency with a nondissipative, traveling wave solution of a biennial frequency,

$$h^* = \sin(t^*) - \sin\left(\frac{t^*}{2} - \frac{x^*}{2}\right) = 2 \sin\left(\frac{t^*}{4} + \frac{x^*}{4}\right) \cos\left(\frac{3t^*}{4} - \frac{x^*}{4}\right) \quad (18)$$

leads to an apparent westward phase speed of 3 (in the nondimensional unit). Like the situation we discussed in the preceding section, the dissipation of the biennial, traveling wave component helps to disconnect the anomalies that appear to propagate at c_r. In (17), the biennial, standing wave component $\sin(t^*/2)$ only acts to modulate the dissipative version of Eq. (18) at a 2-yr period.

In conclusion, a phase speed higher than $2c_r$ is likely to be detected in high latitudes because the annual baroclinic Rossby waves are evanescent there. Although the focus above was on the biennial forcing, the argument can be easily extended to forcings with other interannual frequencies. In fact, combining a standing wave solution of an annual period with any forced solution of a period longer than 1 yr will result in an apparent phase speed greater than $2c_r$. It is in-

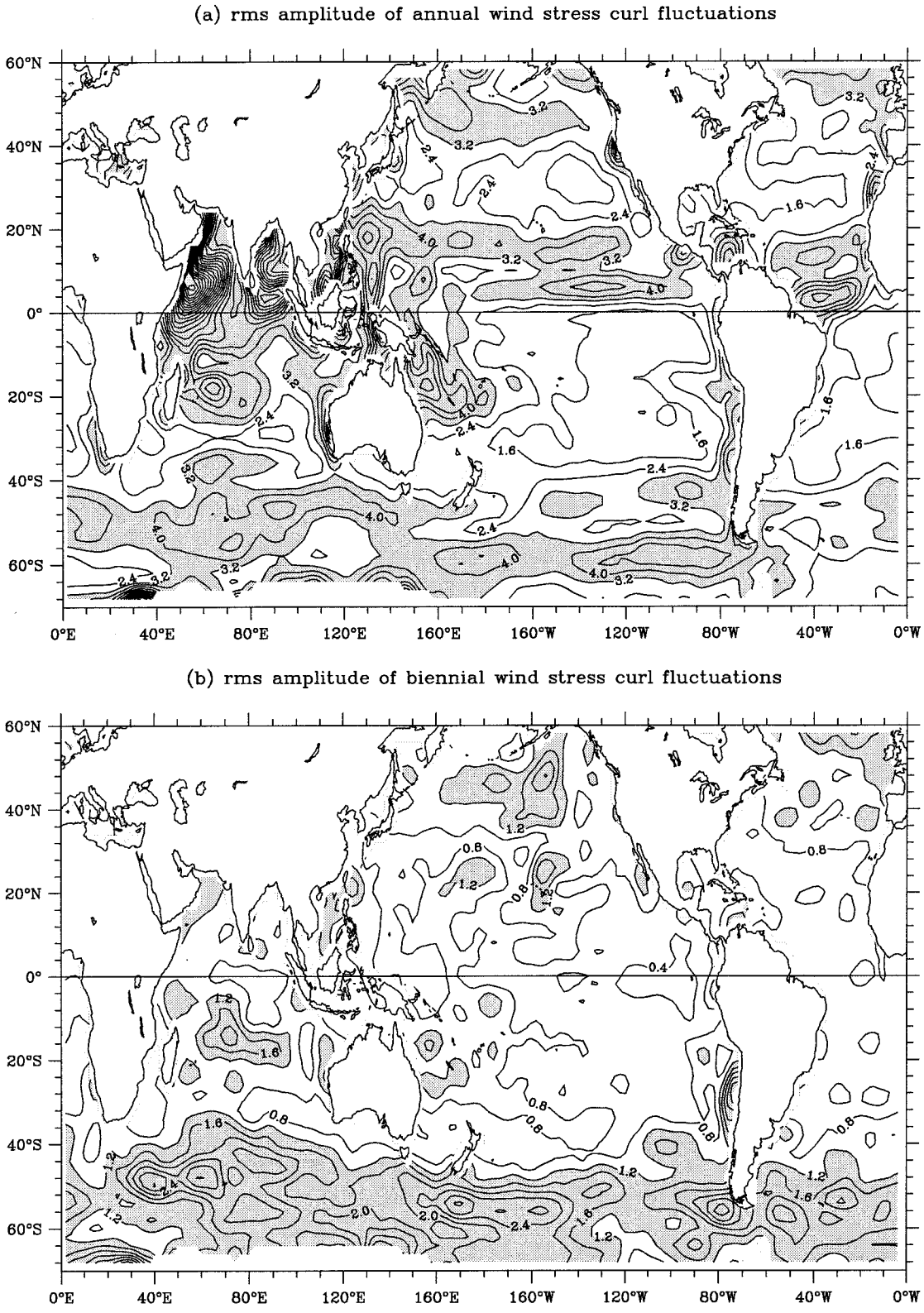

FIG. 9. Rms amplitudes of the wind-stress curl fluctuations in (a) the quasi-annual ($0.8 <$ period < 1.2 yr) and (b) the quasi-biennial ($1.8 <$ period < 2.2 yr) frequency bands. Values (unit in 10^{-8} N m^{-3}) are calculated from the monthly ECMWF wind data from 1985 to 1996. Areas with the rms amplitude values greater than 3.2×10^{-8} N m^{-3} in (a) and 1.2×10^{-8} N m^{-3} in (b) are stippled, respectively.

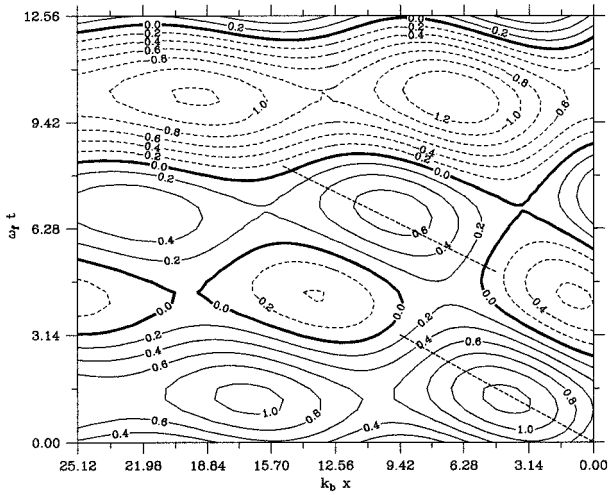

FIG. 10. Time–longitude plot of the h^* pattern in which a standing wave solution of an annual frequency and a forced solution of a biennial frequency are superimposed [see Eq.(17)]. Nondimensional parameters are $x_e k_b = 6\pi$, $\theta^* = 0.2\pi$, and $\alpha^* = 1.2$. Dashed lines denote the westward phase speed at $3c_r$.

teresting to note from Fig. 9 that both the annual and biennial wind fluctuations have higher rms amplitudes in the Southern Hemisphere subpolar regions than in the Northern Hemisphere subpolar regions. A similar result is also found in the other interannual frequency bands of the ECMWF surface wind stress curl data (not shown). This suggests that the coupling between the annually and interannually forced responses should be more evident in the Southern Hemisphere subpolar oceans than in the Northern Hemisphere. The observations presented in Fig. 1, in which phase speeds greater than $2c_r$ appear mostly in the Southern Hemisphere subpolar regions, support this notion.

c. Patterns of surface wind forcing

In all of the cases considered so far, we have assumed that the oscillating surface wind forcing has a constant amplitude A_o within a zonal band $x_b \le x \le 0$ [Eq. (10)]. While solutions are derivable for cases in which A_o is more complicated and x dependent, for example, $A_o \sim \sin(\pi x/x_b)$, this is not pursued here because the uniform-amplitude case presented above contained the essential physics of our interest.

Notice that no restrictions have been placed upon the width of the forcing band x_b. To remove the steric height effect in the observed sea level data, Chelton and Schlax (1996) applied a high-pass filter, passing the off-equatorial sea level signals with zonal scales shorter than $W = 2 \times 10^5\ \theta^{-1}$ km, where θ is the latitude. Such a high-pass filter will remove standing wave signals generated by the uniform-amplitude forcing whose zonal scale x_b is wider than W. For the surface wind forcing with an x-dependent amplitude or if its zonal scale is narrower than W, the forced wave signals will remain in the high-pass filtered sea level data.

5. Summary

In this study, we investigated some of the basic features of the free and forced baroclinic Rossby waves in the off-equatorial oceans. The emphasis has been placed on how eddy dissipation can influence the propagation of the SSH anomalies when both the forced wave response in the interior ocean and the free wave response originating along the ocean's coastal and topographic boundaries are present. This study was motivated by the recent study of Chelton and Schlax (1996), who showed that the phase speed of the SSH anomalies estimated from the TOPEX/POSEIDON altimeter data progressively exceeds the theoretical values as one moves toward higher latitudes. It was also motivated by the common observation that the boundary-generated, baroclinic Rossby waves are highly dissipative in midlatitudes.

The major findings from this study are as follows:

1) The decay scale for the long baroclinic Rossby waves can be evaluated by $x_e \approx -[5\beta(g'H_o)^4/16\omega^4 A_h f^4]^{1/5}$ over most of the off-equatorial oceans for waves having interannual timescales. (If the eddy dissipation is parameterized by Newtonian damping, $x_e \approx -[3\beta(g'H_o)^2/4\omega^2\epsilon f^2]^{1/3}$.) For the baroclinic waves of an annual timescale, this estimation is good equatorward to about 25° lat. Beyond 25° lat, x_e decreases much faster than $f^{-4/5}$, resulting in a highly trapped signal of the baroclinic Rossby waves originating along the ocean's eastern boundary in midlatitude regions.
2) Within the ocean's interior, a large-scale wind forcing induces both a standing wave response and a traveling wave response. The combined wave pattern thus induced favors the phase speed of the free baroclinic wave c_r, if no dissipation is considered. When eddy dissipation is present, we found the forced wave pattern appears to propagate westward at $2c_r$ at all the off-equatorial regions. The appearance of the doubled phase speed is due to the fact that the traveling-wave response is subject to eddy dissipation, while the forced response is not.
3) When both the boundary-generated free waves and the interior-forced wave motions are present, we found the former can strengthen the $1c_r$ phase propagation in the combined height anomaly patterns. This strengthening is most effective in low latitudes where the boundary-generated free waves are less subject to eddy dissipation; it becomes progressively less effective as one moves poleward because of the increasing shortening of the free wave's decay scale. Toward the higher latitude, the forced wave motion, which has an apparent phase

speed of $2c_r$, becomes progressively more dominant.

4) In high latitude regions where the annual Rossby waves are evanescent (poleward of about 40°), baroclinic Rossby waves with an interannual timescale play an important role for the propagating signals. Coexistence of an annual standing wave response and a propagating Rossby wave with an interannual period can result in an apparent phase speed higher than $2c_r$ in the subpolar regions. Because the annual and interannual wind fluctuations in the Southern Hemisphere subpolar regions are stronger than in the Northern Hemisphere subpolar regions, the apparent phase speed higher than $2c_r$ is more likely to be detected in the Southern Hemisphere subpolar oceans. This notion is consistent with the observations shown in Fig. 1.

Finally, although no attempt is made in this study to reproduce the trend shown in Fig. 1, we believe the results summarized above provide one possible mechanism that helps explain the observed features from the newly available T/P altimeter data.

Acknowledgments. This study benefited from an insightful presentation by Dudley Chelton at a T/P Science Working Team Meeting in Southampton, U.K. Careful reading and detailed comments made by Chris Hughes, Bill Kessler, Liping Wang, and an anonymous reviewer helped clarify many parts of an early version of the manuscript. The monthly ECMWF wind stress data was generously provided to us by NCAR. Support from NSF through Grant OCE94-03048, from NASA through the Young Investigators Award NAGW-5250 (BQ, WM), and from ONR (PM) is gratefully acknowledged.

APPENDIX

Decay of Free Baroclinic Rossby Waves Under Newtonian Damping

The momentum dissipation in section 2 was assumed in the form of horizontal eddy diffusion. An alternative way to parameterize the momentum dissipation is through Newtonian damping. This is achieved by replacing the dissipation terms $A_h\nabla^2 u$ and $A_h\nabla^2 v$ in Eqs. (1)–(2) by $-\epsilon u$ and $-\epsilon v$, respectively. Here, ϵ is the Newtonian damping coefficient. For $\epsilon \leq O(100\ \text{days}^{-1})$, we can derive the following dispersion relation for the dissipative, long baroclinic Rossby waves in the same fashion as we derived Eq. (6):

$$k \approx k_b + i\frac{\epsilon}{\beta}(l^2 + k_b^2), \tag{A1}$$

where k_b, β, and l have the same definitions as in Eq. (6).

Similar to the case with the horizontal eddy diffusion parameterization, we can estimate the *e*-folding distance in this case by solving

$$\frac{\epsilon\omega^2}{\beta c_r^2}\int_0^{x_e}\left[\left(\frac{2\beta x}{f}\right)^2 + 1\right]dx = -1. \tag{A2}$$

In latitudes where $x_e \gg f/2\beta$, the *e*-folding scale can be approximated by

$$x_e \approx -\left[\frac{3\beta(g'H_o)^2}{4\omega^2\epsilon f^2}\right]^{1/3}. \tag{A3}$$

Figure A1 shows the x_e values under a biennial forcing given different Newtonian damping timescales. The latitudinal dependence of x_e is very similar to the horizontal eddy diffusion parameterization case shown in Fig. 4b, indicating that expressing the momentum dissipation by Newtonian damping, instead of horizontal eddy diffusion, will not alter the conclusions reached in this study.

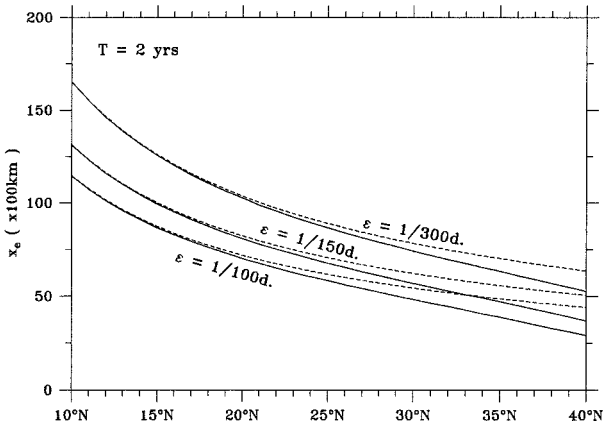

FIG. A1. Same as in Fig. 4b except that the eddy dissipation is expressed in the form of Newtonian damping. The Newtonian damping timescales here range from 1/100 days to 1/300 days. Dashed lines denote the approximate solution of Eq. (A3) and solid lines denote the exact solution from Eq. (A2).

REFERENCES

Barnier, B., 1988: A numerical study of the influence of the Mid-Atlantic Ridge on nonlinear first-mode baroclinic Rossby waves generated by seasonal wind. *J. Phys. Oceanogr.*, **18,** 417–433.

Chao, Y., and L.-L. Fu, 1995: A comparison between the TOPEX/POSEIDON data and a global ocean circulation model during 1992–1993. *J. Geophys. Res.*, **100,** 24 965–24 976.

Chelton, D. B., 1996: Observations and modeling of baroclinic Rossby waves. *Abstracts of TOPEX/Poseidon Science Working Team,* Southampton, United Kingdom, 26.

——, and M. G. Schlax, 1996: Global observations of oceanic Rossby waves. *Science,* **272,** 234–238.

Jacobs, G. A., W. J. Emery, and G. H. Born, 1993: Rossby waves in the Pacific Ocean extracted from Geosat altimeter data. *J. Phys. Oceanogr.*, **23,** 1155–1175.

Jenkins, W. J., 1991: Determination of isopycnal diffusivity in the Sargasso Sea. *J. Phys. Oceanogr.*, **21,** 1058–1061.

Kang, Y. Q., and L. Magaard, 1980: Annual baroclinic Rossby

waves in the central North Pacific. *J. Phys. Oceanogr.,* **10,** 1159–1167.

Kessler, W. S., 1990: Observations of long Rossby waves in the northern tropical Pacific. *J. Geophys. Res.,* **95,** 5183–5217.

——, and J. P. McCreary, 1993: The annual wind-driven Rossby wave in the subthermocline equatorial Pacific. *J. Phys. Oceanogr.,* **23,** 1192–1207.

Killworth, P. D., D. B. Chelton, and R. A. de Szoeke, 1997: The speed of observed and theoretical long extra-tropical planetary waves. *J. Phys. Oceanogr.,* **27,** 1946–1966.

Levitus, S., and T. Boyer, 1994: *World Ocean Atlas 1994.* Vol 4: *Temperature, NOAA Atlas NESDIS 4,* U.S. Govt. Printing Office, 117 pp.

——, R. Burgett, and T. Boyer, 1994: *World Ocean Atlas 1994.* Vol 3: *Salinity, NOAA Atlas NESDIS 3,* U.S. Govt. Printing Office, 99 pp.

McCreary, J. P., 1977: Eastern ocean response to changing wind systems. Ph.D. thesis, University of California, San Diego, 156 pp.

——, P. K. Kundu, and S. Chao, 1987: On the dynamics of the California Current system. *J. Mar. Res.,* **45,** 1–32.

Meyers, G., 1979: On the annual Rossby wave in the tropical North Pacific Ocean. *J. Phys. Oceanogr.,* **9,** 664–673.

Wang, L., and C. J. Koblinsky, 1994: Influence of mid-ocean ridges on Rossby waves. *J. Geophys. Res.,* **99,** 25 143–25 153.

White, W., 1977: Observations of long Rossby waves in the northern tropical Pacific. *J. Phys. Oceanogr.,* **7,** 50–61.

——, 1985: The resonant response of interannual baroclinic Rossby waves to wind forcing in the eastern midlatitude North Pacific. *J. Phys. Oceanogr.,* **15,** 403–415.

——, Y. Chao, and C.-K. Tai, 1997: Coupling of oceanic Rossby waves with the atmosphere in the Pacific basin. *J. Phys. Oceanogr.,* in press.